Nickel Foam Supported Porous Copper Oxide Catalysts with Noble Metal-like Activity for Aqueous Phase Reactions

ARTICLE

Nickel Foam Supported Porous Copper Oxide Catalysts with Noble Metal-like Activity for Aqueous Phase Reactions

Lorianne R. Shultz,[a] Konstantin Preradovic,[a] Suvash Ghimire,[b] Hayden M. Hadley,[a] Shaohua Xie,[c] Varchaswal Kashyap,[b] Melanie J. Beazley,[a] Kaitlyn E. Crawford,[a,b,c,d] Fudong Liu,*[c,e,f] Kausik Mukhopadhyay,*[b] Titel Jurca*[a,c,f]

Contiguous metal foams offer a multitude of advantages over conventional powders as supports for nanostructured heterogeneous catalysts; most critically a preformed 3-D porous framework ensuring full directional coverage of supported catalyst, and intrinsic ease of handling and recyclability. Nonetheless, metal foams remain comparatively underused in thermal catalysis compared to more conventional supports such as amorphous carbon, metal oxides, zeolites and more recently MOFs. Herein, we demonstrate a facile preparation of highly-reactive, robust, and easy to handle Ni foam-supported Cu-based metal catalysts. The highly sustainable synthesis requires no specialized equipment, no surfactants or additive redox reagents, uses water as solvent, and $CuCl_2(H_2O)_2$ as precursor. The resulting material seeds as well-separated micro-crystalline $Cu_2(OH)_3Cl$ evenly covering the Ni foam. Calcination above 400 °C transforms the $Cu_2(OH)_3Cl$ to highly porous CuO. All materials display promising activity towards the reduction of 4-nitrophenol and methyl orange. Notably, our leading CuO-based material displays 4-nitrophenol reduction activity comparable with very reactive precious-metal based systems. Recyclability studies highlight the intrinsic ease of handling for the Ni foam support, and our results point to a very robust, highly recyclable catalyst system.

1. Introduction

Metal foams as thermal catalyst supports are a staggeringly underused platform compared to more conventional supports such as porous amorphous or nanostructured carbonaceous materials,[1,2] metal oxides,[3,4] zeolites,[5] and more recently MOFs.[6,7] Yet foams offer numerous advantages such as a preformed macroporous 3-D framework ensuring full directional coverage of catalyst (Fig. 1a), and an inherently contiguous structure. The latter offers many advantages such as: ease of manipulation, and circumvention of additional steps typically required to pack, adhere, and deliver powder systems (Fig. 1b).[8-12] Additional advantages of Ni foams specifically is their ability to undergo resistive heating,[13] and their ferromagnetism, which renders them self-stirring (Fig. 1c). While this may seem trivial, stirring is critical for mass transport

in applied lab-scale catalysis, and use of stir bars with fragile nano-structured materials (e.g. catalysts supported on graphene foams)[14] can damage the catalyst structure impairing recoverability which leads to both poor recyclability and contamination of product. Furthermore, a recent report from Ananikov and coworkers highlighted the propensity of contaminated PTFE-coated stir bars to promote catalytic reactions leading to false positives.[15] Removing the stir bar from the equation allows for an unadulterated study of catalyst performance.
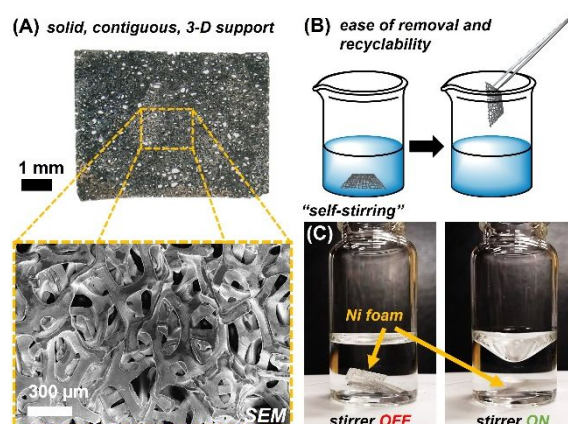
Fig. 1 (a) Optical and SEM micrographs of Ni foam. Highlighting ease of recovery (b), and stirring enabled by the Ni foam support (c; no stir bars, 300 rpm).

Department of Chemistry, University of Central Florida, Orlando, Florida, 32816 (USA), E-mail: Titel.Jurca@ucf.edu

b.   *Department of Materials Science and Engineering, University of Central Florida Orlando, Florida, 32816 (USA), E-mail: Kausik@ucf.edu*

c.   *NanoScience and Technology Center (NSTC), University of Central Florida Orlando, Florida, 32826 (USA)*

d.   *Biionix Faculty Cluster, University of Central Florida, Orlando, Florida, 32816 (USA)*

e.   *Department of Civil, Environmental, and Construction Engineering, University of Central Florida, Orlando, Florida, 32816 (USA) E-mail: Fudong.Liu@ucf.edu*

f.   *Renewable Energy and Chemical Transformation Faculty Cluster (REACT), University of Central Florida, Orlando, Florida, 32816 (USA)*

The majority of work utilizing metal foams for catalysis to date focuses on electrochemical applications; for example, water splitting,[16-22] ammonia electrooxidation,[23] oxidation of methanol to formate,[24] hydrazine oxidation,[25] and H_2O_2 electroreduction.[26] Their use in conventional thermal catalysis is by comparison, vastly underexplored. Nonetheless, metal foam supports have been successfully utilized for a number of applications, including sodium borohydride alcoholysis,[27] NO_x reduction,[28] formaldehyde oxidation,[29] polystyrene hydrogenation,[30] catalytic combustion of CH_4,[31] and catalytic oxidation of CO.[32] Such examples highlight the broad-scope utility of metal foams and provides motivation for their continued implementation in catalyst design.

The reduction of nitroaromatics, and azo dyes has garnered significant interest in the past two decades. Specifically, due to the ease and reliability of tracking such reactions, typically the reduction of 4-nitrophenol (**4NP**), by UV-Vis spectroscopy, they have become a standard protocol for validating thermal redox activity for heterogeneous and nano-catalysts.[33,34] The consequence of this is a vast literature database for benchmarking the reactivity of different materials. Concomitantly, nitroaromatics are widely used in the manufacture of pesticides, pigments, dyes, explosives and pharmaceuticals, leading to their release as pollutants in industrial effluent.[35-37] Similarly, azo dyes are found in effluent from the industrial manufacture of plastics, paints, textiles, and cosmetics. These materials pose risks to both the environment and human health, ranging from acute toxicity to either suspected or established carcinogenicity.[38-41] One broadly explored remediation strategy is the aqueous catalytic reduction to yield various anilines, which are both synthetically useful and less toxic.[42]

The majority of related work to date is based on precious and semi-precious metal nanoparticles (e.g. Pd, Pt, Au, Ag, Ru).[43-49] However, in the past decade, systems based on other transition metals,[50-53] and even metal-free systems[54-56] have emerged; typically with comparatively lower reactivity. Many of these catalysts are nanostructured or colloidal in nature, synthesized through complex and often unsustainable routes and can be difficult to recover and reuse. Although their reactivity is often excellent, these factors largely preclude their meaningful application towards pollutant remediation.

Herein we report a facile and highly sustainable route to well-dispersed micro-crystalline $Cu_2(OH)_3Cl$ supported on Ni foam. Subsequent calcination at 400 °C and at higher temperatures yields spatially separate porous CuO on Ni foam. Catalyst testing for the reduction of **4NP** and methyl orange (**MO**) reveals impressive catalytic activity comparable to highly reactive precious metal-based systems. Furthermore, rate is dependent on preparative temperature and varies across **4NP** and **MO**, affording tunability for substrate-specific selectivity. Critically, the catalysts are easy to handle, robust, and readily recyclable.

2. Experimental

2.1 General Methods

All reactions were carried out under air, at ambient temperature (21-23 °C, 45-55% relative humidity). Metal salt $CuCl_2 \cdot (H_2O)_2$ was purchased from Alfa Aesar. Methyl Orange (**MO**) was purchased from Acros Organics. 4-nitrophenol (**4NP**) and $NaBH_4$ were purchased from TCI America. All chemicals were used as received without further purification. Ni foams were purchased from MTI Corporation as 300×80×0.08 mm sheets (99.99%+ purity). Foams were cleaned with 1.0 M HCl, sonication in ethanol, and subsequent rinses with deionized water (DIW) and allowed to dry under vacuum prior to use. UV-Vis Spectra were collected on an Agilent Cary 60 spectrophotometer utilizing 1 cm quartz cuvettes (Spectrocell inc.). Scanning electron microscopy (SEM) images were obtained on a Zeiss Ultra-55 FEG SEM at 2.0-5.0 kV. Energy Dispersive X-ray spectroscopy (EDS) analysis was completed with a Noran System 7 EDS with silicon drift x-ray detector. Optical micrographs were obtained on a Leica DM2500m with an Accu-Scope Excelis-HD camera. Thermogravimetric analysis (TGA) on Ni foam to test for oxidation (mass gain) was conducted on a Shimadzu TGA-50 under lab atmosphere. TGA for mass loss of Cu/Ni_x was conducted on an ISI TGA-1000 with a 5 cc/min flow of ultrahigh purity (UHP) N_2 housed inside an inert atmosphere glovebox operating under UHP N_2. Grazing angle FTIR (GA-FTIR) spectra were acquired on a Shimadzu AIM-9000 FTIR microscope with MCT detector and grazing angle objective coupled with a Shimadzu IRTracer 100 source.

2.2 Materials Synthesis

Solutions of 100 mg [$CuCl_2 \cdot (H_2O)_2$], and 36 pieces of Ni foam (5 x 8 mm) in 50 mL of DIW were heated to 80 °C for 1 h, allowed to cool, removed, and washed with DIW. Isolated foams were dried in a conventional laboratory oven at 100 °C for 1 h, then calcined in a muffle furnace in air at a ramp rate of 3.6 °C/min to reach the respective targets of 200, 300, 400, 500, and 600 °C, where they were held for 1 h. Ni foam blanks to serve as controls in catalysis were also calcined under similar conditions.

2.3 XPS

The X-ray photoelectron spectroscopy (XPS) analyses were carried out with an ESCALAB-250Xi spectrometer an equipped with Al-Kα monochromatic X-ray source (20 mA, 15 kV) and was operated at a power of 300W in ultra-high vacuum pressure chamber ($7×10^{-9}$ mbar) at room temperature, while maintaining the spot size of beam at 650 μm. Binding energy calibrations were done with reference to C 1s peak at 284.6 eV. The Thermo Avantage Peakfit® software was used for the deconvolution of the spectra present in the samples. The spectra were fitted with a Gaussian-Lorentzian peak after the subtraction of a smart background. High-resolution spectra were obtained using either a 10- or 20-eV pass energy, an analysis area of ≈300 × 700 μm, 50-meV step and 60-s sweep intervals. The proper peak fittings were analyzed using an automated incremental peak deconvolution program, which varied the peak heights within an envelope over a complete rage to determine the best fit, checked using the X-squared value to the actual data. See ESI for further details.

2.4 ICP-MS

Solid samples (~2-3 mg) were digested in 3:1 (v/v) nitric acid to hydrochloric acid (trace metal grade; Fisher Scientific) at 85 °C

for 20 minutes until complete dissolution. The solution was diluted 1:100 in ultrapure water (18.2 MΩ.cm) to a 2% (v/v) acidic solution and filtered (0.2 μm pore size) prior to analysis. Dissolved Cu concentrations were measured using a Thermo Fisher Scientific iCap Qc inductively coupled plasma mass spectrometer (ICP-MS) with QCell technology and operated in kinetic energy discrimination (KED) mode of analysis with helium as the collision gas. Calibration, internal, and quality control standards (Inorganic Ventures) were prepared in 2% trace metal grade nitric acid (Fisher Scientific). Scandium and yttrium were used as internal references.

2.5 Surface Area

Nitrogen (N_2) adsorption-desorption isotherm analysis was performed on a Quantachrome Autosorb-iQ physisorption chemisorption instrument. Measurements were performed at 77 K (liquid N_2 bath) on the samples. Prior to testing, the samples were outgassed at 300 °C for 1 h to remove all adsorb molecules from the surface, and the N_2 adsorption–desorption isotherm was measured using pressure intervals of $0 < P/P_0 < 1$ with 20 adsorption steps and 20 desorption steps. Brunauer-Emmett-Teller (BET) method was used to analyze the surface area by using adsorption points in the relative pressures between 0.05 and 0.3.

2.6 Catalysis

Details for catalytic trials are provided in the results and discussion section. For **4NP** reductions, UV-Vis measurements were conducted in the 220-500 nm region. For **MO** reductions, UV-Vis measurements were conducted in the 220-550 nm region. All reactions were conducted under ambient conditions (21-23 °C). Scanning was conducted at fixed intervals using the automated function in the Agilent Cary WinUV software – specific scanning intervals are provided in the Supporting Information section for each set of catalysis trials. Recycling trials were conducted under similar conditions. Samples were rinsed with DIW, ~2 mL/rinse.

3. Results and discussion

3.1 Materials Synthesis and Characterization

Materials were prepared by heating dilute solutions of $[CuCl_2(H_2O)_2]$ (0.012 M) and pre-cut pieces of Ni foam (5 x 8 mm) (Fig. S1) in deionized water (DIW) to 80 °C for 1 h. After cooling to room temperature, the samples were rinsed repeatedly with DIW and dried at 100 °C for 1 h. Samples were subsequently calcined in a muffle furnace in air at a ramp rate of 3.6 °C min^{-1} to reach the respective targets of 200, 300, 400, 500, and 600 °C, where they were held for 1 h. Ni foam blanks to serve as controls for surface area measurements (*vide infra*) were also calcined under similar conditions. The resulting materials were named **Cu/Ni$_x$** (x = calcination temperature in °C). Optical microscopy of samples confirmed even coating of well-separated discrete crystalline material over the entire 3-D foam structure. Notably, **Cu/Ni$_{200}$** (Fig. 2B) and **Cu/Ni$_{300}$** featured green crystallites, while **Cu/Ni$_{400}$**-**Cu/Ni$_{600}$** were coated in dark brown crystalline materials.

All samples were fully characterized by Scanning Electron Microscopy (SEM) with Energy Dispersive X-ray spectroscopy (EDS) to confirm morphology and elemental composition. Samples **Cu/Ni$_{200}$** and **Cu/Ni$_{300}$** featured evenly distributed octahedral crystals predominantly in the 0.5-1.75 μm range along the edge (Fig. 2B,C,S2-3); smaller crystallites, presumably of not fully formed octahedra can also be seen. Sample **Cu/Ni$_{400}$** remarkably maintained the octahedral crystalline shape within the aforementioned size domain, but displayed significant porosity (Fig. 2D,S4). Samples **Cu/Ni$_{500}$** and **Cu/Ni$_{600}$** exhibited a marked degradation in the shape with concomitant increase in calcination temperature. Nonetheless, the materials appeared reasonably well separated commensurate with the original domains occupied by the octahedral crystals – i.e. no evidence of significant sintering is observed (Fig. 2E,S5,S6). Along with the transformation of the Cu-component, the bare Ni foam surface grows an oxide layer (as confirmed by TGA, Fig. S7), which begins to crack and degrade above 500 °C (Fig. S8).
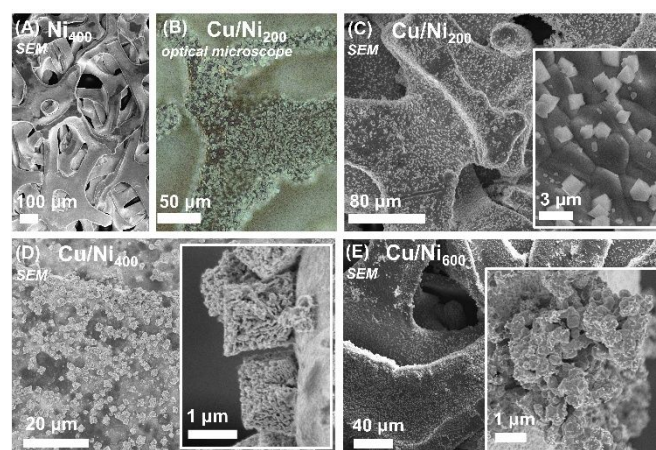
Fig. 2 SEM micrograph of (A) **Ni$_{400}$** blank foam. Optical (B) and SEM (C) micrographs of **Cu/Ni$_{200}$**. Representative SEM micrographs of (D) **Cu/Ni$_{400}$** and € **Cu/Ni$_{600}$** (E). *See ESI for additional images.*

Fig. 3 (A)Thermogravimetric curves for **Cu/Ni$_{200-600}$** conducted under N_2 environment with a heating rate of 20 °C/minute. (B) GA- FTIR spectra for **Cu/Ni$_{200-600}$** highlighting hydroxyl stretching (3300-3600 cm^{-1}) and deformation (700-1000 cm^{-1}) regions.

Fig. 4 X-ray Photoelectron Spectroscopy: (A) survey, (B) O1s and (C) Cu 2p spectra for **Cu/Ni$_{200}$-Cu/Ni$_{600}$**.

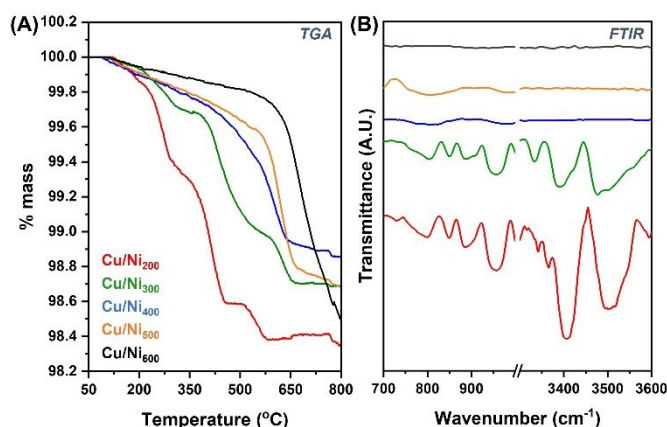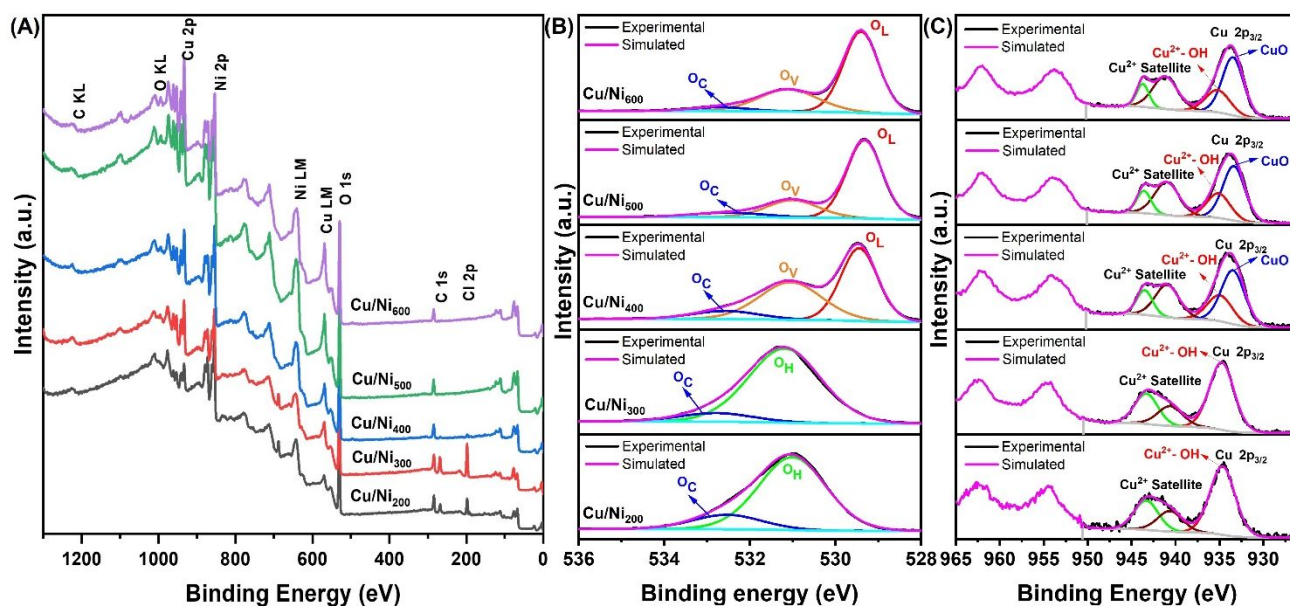During imaging (*vide supra*), SEM-EDS was conducted with the spot size focused predominantly on the Cu-based crystallites. Special attention was given to the Cu:Cl ratio (Table S1). Notably for the green octahedra **Cu/Ni$_{200}$** and **Cu/Ni$_{300}$**, ratios of 2.3(±0.5):1 and 2.4(±0.4):1 respectively were observed. Based on this ratio and the color profile, we postulate the species to be Cu$_2$(OH)$_3$Cl. **Cu/Ni$_{400}$-Cu/Ni$_{600}$** exhibited ratios of 29.8(±9.2):1, 72.8(±1.0):1, and 66.5(±1.0):1. Based on observed color profile and literature precedent, this is commensurate with the thermolysis of Cu$_2$(OH)$_3$Cl to yield CuO.

Thermogravimetric analysis (TGA) of all materials was conducted under an N$_2$ environment inside a glovebox to negate any potential oxidation effects which would complicate the detection of the small amounts of Cu-based material present. The samples were heated at 20 °C min^{-1} from 25 °C to 800 °C (Fig. 3). TGA curves of **Cu/Ni$_{200}$** and **Cu/Ni$_{300}$** both displayed multi-step curves characteristic for Cu$_2$(OH)$_3$Cl;[57] step 1 **Cu/Ni$_{200}$** (145 °C – 295 °C) and **Cu/Ni$_{300}$** (150 °C – 305 °C), step 2 **Cu/Ni$_{200}$** (295 °C – 455 °C) and **Cu/Ni$_{300}$** (305 °C – 520 °C), and step 3 **Cu/Ni$_{200}$** (455 °C – 580 °C) and **Cu/Ni$_{300}$** (520 °C – 700 °C). TGA curves of **Cu/Ni$_{400}$**, **Cu/Ni$_{500}$** and **Cu/Ni$_{600}$** displayed single-step curves characteristic for CuO;[58] **Cu/Ni$_{400}$** (145 °C – 640 °C), **Cu/Ni$_{500}$** (145 °C – 665 °C) and **Cu/Ni$_{600}$** (145 °C – 800+ °C). Notably, the mass loss region for each observed step in the TGA curves shifted to higher temperatures, commensurate with the increased calcination temperature used to prepare the material, even among comparable materials (i.e., Cu$_2$(OH)$_3$Cl and CuO based systems, respectively). We postulate this is due to the formation of a stronger interaction with the Ni foam surface, and the likely formation of Ni-Cu alloying (*vide infra*).

To corroborate the presence of Cu$_2$(OH)$_3$Cl and CuO in **Cu/Ni$_{200-300}$** and **Cu/Ni$_{400-600}$** respectively, FTIR analysis was conducted. Grazing angle reflectance FTIR (GA-FTIR) measurements were collected using a 50 × 50 μm spot size, and native Ni foam as the subtracted background (Fig. 3B). Analysis

of the hydroxyl stretching (3300-3600 cm^{-1}) and deformation (700-1000 cm^{-1}) regions revealed the expected characteristic peaks of Cu$_2$(OH)$_3$Cl for **Cu/Ni$_{200-300}$** and absence thereof for CuO in **Cu/Ni$_{400-600}$**.[59]

To further validate the proposed identity of the materials, x-ray photoelectron spectroscopy (XPS) was conducted (Fig. 4A). Further details are provided in the supporting information (pg S10-S14). The C 1s high-resolution spectrum of samples was deconvoluted into three peaks, and the main peak of the C 1s spectrum was fitted for adventitious carbon at binding energy (BE) value of 284.8 eV with the Gaussian-Lorentzian peak fit method (Fig. S9). The surface composition and relative atomic percentage of the elements present in the survey spectrum are shown in Table S2. The BE values for Cu 2p and Ni 2p species decreased with the increase in annealing temperatures and increased Cu concentration. The increased Cu concentration is related to the gradual transition from Cu$_2$(OH)$_3$Cl (70% Cu) to CuO (80% Cu) going from **Cu/Ni$_{200}$** to **Cu/Ni$_{600}$** (Fig. 4) The shift in the BE values due to the increased Cu content can also suggest possible formation of NiCu solid solution, or alloy at the Ni-Cu interface.[60] Overall, we observe a decrease in the Cl:Cu ratio from **Cu/Ni$_{200}$-Cu/Ni$_{400}$**, with complete disappearance of Cl signal for **Cu/Ni$_{500}$** and **Cu/Ni$_{600}$**. For **Cu/Ni$_{200}$** and **Cu/Ni$_{300}$**, the chlorine (Cl) peak present along with the BE values of Cu 2p$_{3/2}$ are consistent with the proposed Cu$_2$(OH)$_3$Cl, wherein Cu^{2+} is bonded to Cl$^-$ ions.[61] Similarly, the Cl peaks observed for **Cu/Ni$_{400}$** represent residual surface bound chlorides (Cu^{2+} species) formed by release of HCl upon calcination (*vide infra*).

Moreover, we analyzed the O 1s spectra, which discloses the gradual changes in the catalyst samples with respect to annealing temperatures (Fig. 4B). The O 1s spectrum can be resolved into two and three components (Fig. 4B). The samples annealed at lower temperature, **Cu/Ni$_{200}$** and **Cu/Ni$_{300}$**, are deconvoluted into two peaks centered at 531.01 ± 0.18 eV and 532.53 ± 0.26 eV and are assigned to hydroxide and chemically

adsorbed oxygen (O_C).[62] However, the samples annealed at higher temperature have been deconvoluted into three peaks centered at 529.33 $\pm$ 0.12 eV, 531 $\pm$ 0.1 eV, and 532.51 $\pm$ 0.19 eV and assigned to lattice oxygen, oxygen vacancy (O_V), and adsorbed oxygen (O_C) respectively.[63] Notably, O_V, as conventionally discussed, does not represent the direct detection of oxygen vacancies; rather, it is the detection of adsorbed O^-, O_2^-, and -OH groups trapped in formal oxygen vacancies in the material, as it has been previously reported.[64-67] The O_C component at higher binding energy (532.51 – 532.79 eV) is attributed to chemisorbed and dissociated oxygen species.[68] The relative proportion of O_C components has decreased from 16.96 % to 4.96 % as the annealing temperature increased from 200 to 600 °C (Table S5). This suggests the removal of adsorbed oxygen from the sample surface at a higher temperature. The O_L peak at 529.33 $\pm$ 0.12 eV of the samples at elevated temperature ($\geq$ 400 °C) suggested the presence of a metal-oxygen bond, likely the presence of copper and nickel oxide.[69]

Apart from the above deconvoluted spectra, the Cu core level XPS analysis was conducted. Figure 4C compares the Cu 2p peaks of **Cu/Ni$_{200}$-Cu/Ni$_{600}$**. The Cu $2p_{3/2}$ spectra of **Cu/Ni$_{200}$** and **Cu/Ni$_{300}$** are deconvoluted into one main peak centered at 934.65 $\pm$ 0.08 eV, and corresponding satellite peaks at 940.61 $\pm$ 0.03 eV and 943.32 eV. However, at elevated annealing temperature ($\geq$ 400 °C), the Cu $2p_{3/2}$ spectra are deconvoluted into two main peaks (933.36 $\pm$ 0.14 eV and 934.65 $\pm$ 0.45 eV) and corresponding satellite peaks (940.95 $\pm$ 0.13 eV and 943.51 $\pm$ 0.22 eV). The Cu $2p_{3/2}$ spectra at 934.65 - 935. 20 eV are assigned to Cu^{2+}-OH species, suggesting the possibility of the presence of $Cu(OH)_2$, or $Cu_2(OH)_3Cl$ species.[70] Similarly, the Cu $2p_{3/2}$ spectra at 933.36 $\pm$ 0.14 eV at elevated annealing temperature have been assigned to Cu^{2+}-oxide (i.e., CuO).[61] The increased Cu^{2+}-oxide peak intensity and decreased Cu^{2+}-OH peak intensity are consistent with the transition of hydroxide to oxide at elevated temperatures. Additionally, the ratio of intensity of Cu $2p_{3/2}$ to shake-up satellite intensity ($I_{Cu2p3/2}/I_{shake-up}$) is an important tool to determine the oxidation states of Cu present in the sample by BE values. This is considered a predictor for Cu^+ species present in the sample. As from the literature, if there is an increase in Cu $2p^{3/2}$ peak intensities and decrease in corresponding Cu $2p^{3/2}$ satellite peak intensities, then Cu^+ species are supposed to be present in the sample.[71] In our systems, when the calcination temperature was increased from 200 to 600 °C, there were no noticeable changes in the intensities of Cu $2p_{3/2}$ peak and its corresponding satellite peaks. This finding is consistent with the presence of Cu^{2+} species ($Cu_2(OH)_3Cl$, CuO, and surface $Cu(OH)_2$) and rules out the presence of Cu_2O (i.e. Cu^+ species).

For the exposed Ni foam, increasing annealing temperature changes the Ni-OH surface species to NiO at higher temperature (400 °C and above, **Cu/Ni$_{400}$-Cu/Ni$_{600}$**) owing to the condensation reactions between the neighboring (Ni)-

hydroxide groups at elevated temperatures. This accounts for the relatively larger presence of NiO molecules (atomic concentration %) instead of Ni-OH species on the catalyst surfaces when annealed at higher temperatures (400+ °C) as observed from the BE values in the XPS spectrum (see Tables S3,S6).

Based on EDS, TGA, FTIR and XPS measurements, the crystalline materials grown on the foams are assigned as $Cu_2(OH)_3Cl$ (**Cu/Ni$_{200}$, Cu/Ni$_{300}$**) and CuO (**Cu/Ni$_{400}$-Cu/Ni$_{600}$**). Therein, we tentatively ascribe the initial formation of $Cu_2(OH)_3Cl$ to eq. (1), where terminal Ni-OH species facilitated the reaction of dissolved $CuCl_2$ to form $Cu_2(OH)_3Cl$.[72] The product then seeds on the Ni foam surface and continues growing, according to eq. (2), to form octahedral crystals (0.5-1.75 µm) of $Cu_2(OH)_3Cl$. It is likely that surface Ni-OH groups react further with -Cl groups on the basal plane of the seeding crystallites to further immobilize the material on the surface. We postulate, based on observed stability of the materials and XPS analysis, that this leads to Ni-Cu alloying at the foam-crystallite interface upon annealing (*vide supra*). Calcination under air (54% relative humidity) at 400 °C and above led to the formation of CuO likely according to two competing processes; aided by ambient O_2 with concomitant release of Cl_2 and H_2O (eq. 3), or via decomposition with release of HCl and H_2O (eq. 4)[57,73] and formation of pores in the octahedral structure (Fig. 5). It is expected that release of HCl would leach some Cu-based material, and this is indeed observed by ICP-MS (Table 1) where there is a significant decrease in %Cu content going from **Cu/Ni$_{200-300}$** to **Cu/Ni$_{400-600}$** (respectively 2.3% w/w avg. to 1.3% w/w avg.). Based on EDS, TGA, and XPS data, the % Cu content was used to assign the % of respective Cu species ($Cu_2(OH)_3Cl$, CuO) in the sample (Table 1).

(1) $\quad 2\ CuCl_2 + 3\ Ni_{foam}\text{-}OH + H_2O \rightarrow Cu_2Cl(OH)_3 + 3\ Ni_{foam}^+ + 3Cl^-$

(2) $\quad 2\ CuCl_2 + 3\ H_2O \rightarrow Cu_2Cl(OH)_3 + 3\ H^+ + 3Cl^-$

(3) $\quad 2\ Cu_2Cl(OH)_3 \cdot 8H_2O + \tfrac{1}{2}O_2 \rightarrow 4\ CuO + Cl_2 + 19\ H_2O$

(4) $\quad Cu_2Cl(OH)_3 \rightarrow 2\ CuO + HCl + H_2O$
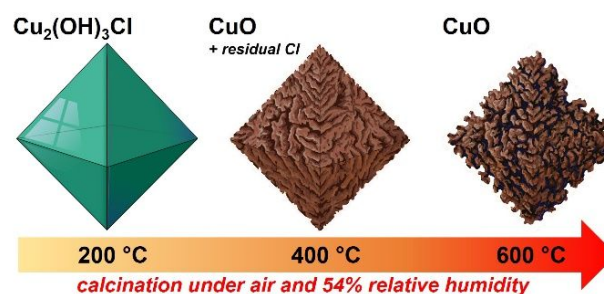
Fig. 5 Graphical representation for the formation of $Cu_2(OH)_3Cl$ crystals on Ni foam support followed by the conversion to CuO and gradual formation of porous structure by calcination under lab atmosphere.

Given the notable porosity of **Cu/Ni$_{400}$-Cu/Ni$_{600}$** (Fig. 2D,E), we sought to determine the relative surface area of the Cu-based component of the materials. This proved challenging given the inherent inhomogeneity of the materials in general (i.e. randomized pores in the Ni foam), and the fact that the highly porous Cu species represent only a small fraction of the over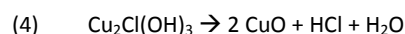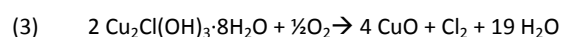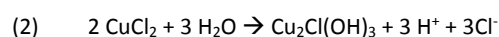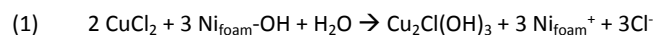all material mass. Notably, the core Ni foam material is itself a 3-D material with inherent macroporisity. Thus, to approximate we measured the difference in surface area between **Cu/Ni$_x$** and **Ni$_x$**, thereby accounting for changes to surface area on the bare Ni foam as a result of calcination, and utilized the derived % mass of the proposed Cu material (*vide supra*) to assign the resulting surface area of the Cu-based component.

Nitrogen (N$_2$) adsorption-desorption isotherm analyses were performed at 77 K (liquid N$_2$ bath) on the samples. Prior to testing, the samples were outgassed at 300 °C for 1 h to remove all adsorbed molecules from the surface, and the N$_2$ adsorption–desorption isotherms were measured using pressure intervals of 0 < P/P$_0$< 1 with 20 adsorption steps and 20 desorption steps (Fig. S12, S13). The Brunauer-Emmett-Teller (BET) method was used to analyze the surface area by using adsorption points in the relative pressures between 0.05 and 0.3. Several samples of **Cu/Ni$_x$** were utilized at each temperature and averaged. The inhomogeneity between samples is reflected in the relatively high errors (Table 1). Notably, the % error becomes dramatically less as the material identity transitions from Cu$_2$(OH)$_3$Cl to CuO, which is commensurate with the notable appearance of nano-sized pores in the SEM micrographs (Fig. 2). The relatively high BET surface areas of the CuO materials (**Cu/Ni$_{400}$-Cu/Ni$_{600}$**) averages 805 ± 250 m^{2}g^{-1}, in line with the formation of mesopores within the material. The high surface area of the CuO components is promising for potential application in catalysis.
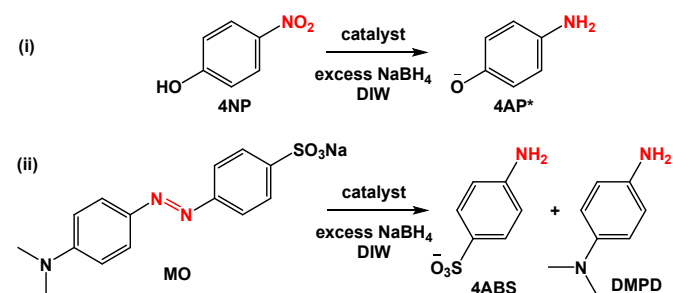
Table 1 %Cu composition (w/w) obtained by ICP-MS, %Cu species normalized to proposed identities (*a* = Cu$_2$(OH)$_3$Cl; *b* = CuO), and extrapolated BET surfaces areas of the Cu-based component.

Material	%Cu(ICP-MS)	%Cu species	Surface Area (m^{2}g^{-1})
Cu/Ni$_{200}$	1.877	*a*3.154	202.4 ± 119.2
Cu/Ni$_{300}$	2.727	*a*4.583	184.4 ± 126.1
Cu/Ni$_{400}$	1.435	*b*1.796	842.1 ± 170.3
Cu/Ni$_{500}$	1.069	*b*1.338	689.4 ± 261.7
Cu/Ni$_{600}$	1.318	*b*1.649	885.9 ± 319.3

3.2 Catalyst Testing

To benchmark the catalytic activity for these Ni$_{foam}$-supported materials, we turned to nitroarene and azo dye reduction reactions. These reaction systems are ubiquitous for testing thermal redox-type heterogeneous catalysts and offer a facile means of comparison to the broader literature.[36-38] Reaction progress is readily tracked by UV-Vis spectroscopy, allowing for measurements to be carried out in-situ (in the quartz cell). Employing a general protocol our group has previously optimized, 0.39 μmol 4-nitrophenol (**4NP**) or 0.34 μmol methyl orange (**MO**) was dissolved in 1 mL of DIW and mixed with a 2 mL solution of 0.2 mmol NaBH$_4$.[74] The over 500-fold excess of NaBH$_4$ creates a pseudo-first order process, greatly simplifying

the extraction of kinetics. Reaction of **4NP** with BH$_4$$^-$ generates 4-nitrophenolate (**4NP***) marked by a bright yellow color, and a red shift from λ_{max} = 317 nm to λ_{max} = 400 nm. Catalytic reduction furnishes the product 4-aminophenolate (**4AP***) accompanied by decolorization and the appearance of a lower intensity peak at λ_{max} = 310 nm (Scheme 1). In a similar manner, the bright yellow/orange solution of **MO**, λ_{max} = 464 nm is hydrogenated to a mixture of colorless products 4-aminobenzene sulfonic acid (**4ABS**) λ_{max} = 254 nm, and N,N-dimethyl-p-phenylene-diamine (**DMPD**) at λ_{max} = ~245 nm and ~305 nm; the latter are poorly resolved due overlap with **4ABS** (Scheme 1).[74-76]

Scheme 1 Catalytic (**Cu/Ni$_x$**) reduction of: (i) **4NP** to **4AP*** in DIW with large excess NaBH$_4$, tracked by UV-Vis by decrease of **4NP*** peak (λ_{max} = 400 nm); (ii) **MO** to **4ABS** + **DMPD** in DIW with large excess NaBH$_4$, tracked by UV-Vis by decrease of **MO** peak (λ_{max} = 464 nm).

Table 2 Catalytic (**Cu/Ni$_{xx}$**) reduction of **4NP** to **4AP** and **MO** to **4ABS** and **DMPD** in DIW with large excess NaBH$_4$. Observed rates normalized to %Cu species (w/w). *Error presented as ± std. dev.; *normalized to mass of Ni foam for blank trials.*

Catalyst	Catalyst order	Substrate	K_{avg} [min^{-1}(g Cu-cat)$^{-1}$]
Cu/Ni$_{200}$	*first*	**4NP**	4165.1 ± 166.4
Cu/Ni$_{300}$	*first*	**4NP**	154825.0 ± 86738.0
Cu/Ni$_{400}$	*first*	**4NP**	15056.6 ± 3827.1
Cu/Ni$_{500}$	*first*	**4NP**	714351.0 ± 15626.3
Cu/Ni$_{600}$	*first*	**4NP**	283968.0 ± 4257.7
Ni$_{200}$	*first*	**4NP**	1.2*
Ni$_{400}$	*first*	**4NP**	5.1*
Cu/Ni$_{200}$	*last*	**4NP**	1826.4 ± 361.0
Cu/Ni$_{300}$	*last*	**4NP**	394.7 ± 26.7
Cu/Ni$_{400}$	*last*	**4NP**	2338.8 ± 489.9
Cu/Ni$_{500}$	*last*	**4NP**	4967.0 ± 350.7
Cu/Ni$_{600}$	*last*	**4NP**	4257.7 ± 1413.1
Ni$_{200}$	*last*	**4NP**	2.7*
Ni$_{600}$	*last*	**4NP**	4.6*
Cu/Ni$_{200}$	*last*	**MO**	13474.9 ± 1992.3
Cu/Ni$_{300}$	*last*	**MO**	3600.6 ± 286.6
Cu/Ni$_{400}$	*last*	**MO**	23676.0 ± 1819.8
Cu/Ni$_{500}$	*last*	**MO**	20752.0 ± 2151.0
Cu/Ni$_{600}$	*last*	**MO**	6615.4 ± 124.9
Ni$_{400}$	*last*	**MO**	88.5*

Utilizing UV-Vis measurements, catalyst performance is quantified in terms of the apparent rate constant k_{app} (Eq. 5). Therein, k_{app} is derived from the slope of ln(C/C_0) as a function

of time, where C/C_0 is obtained from the absorbance of the starting material (e.g., **4NP*** at λ_{max} = 400 nm, **MO** at λ_{max} = 464 nm) (A/A_0)), collected after an induction period (*in some cases, not observed on the time interval scale of measurements*). The details governing kinetics extraction based on this approximation have been discussed at length in prior literature.[33, 34, 77,78]

(5)

$$-k_{app}t = ln\left(\frac{A}{A_0}\right) = ln\left(\frac{C}{C_0}\right)$$

For **4NP** reduction, reactions were conducted with two different orders of addition. In the *catalyst first* approach, components were introduced in the order: catalyst, **4NP** in 1 mL DIW, and NaBH$_4$ in 2 mL DIW. The solution was stirred for ~2 seconds, and scans were obtained at fixed intervals. A stock solution of all components, sans-catalyst was used as the surrogate t_0 reference for C_0. With the *catalyst last* order of addition, components were introduced in the order: **4NP** in 1 mL DIW, NaBH$_4$ in 2 mL DIW, stirred and obtained t_0 scan, then catalyst. The solution was stirred for ~2 seconds, and scans were obtained at fixed intervals. The *catalyst last* approach which results in slower reactivity, and lower solution turbidity (from H$_2$ evolution due to NaBH$_4$ hydrolysis) was employed for **4NP** recycling trials (*vide infra*), and the reduction of **MO**. To ascertain the contribution of reactivity from the Ni foam support, bare foams calcined at 200 and 400 °C (**Ni$_{200}$**, **Ni$_{400}$**) were tested for catalytic reduction of **4NP**. The foams showed no/extremely low activity in the 45 min. testing time with both orders of addition evaluated. In the case of **MO**, **Ni$_{400}$** revealed only low reactivity in the 25 min. tested (Table 2, Fig. 6). Because the foam support proved to be a poor catalyst for **MO**, and a negligible contributor for **4NP**, catalytic rates obtained for **Cu/Ni$_x$** were normalized to the weight of the associated Cu species (Table 1). Thus, k_{app} is converted to K [min^{-1}(g Cu-cat)$^{-1}$]. Multiple trials were conducted for each material (pg. S16-S20) and the average normalized rate (K_{avg}) reported (Table 2, Fig. 6). It should be noted that although the Ni foam does not appear to promote catalysis on its own, the role of synergism between the Cu species and the support cannot be ruled out in this current study.

In general, the *catalyst first* order of addition yielded dramatically higher rates than the *catalyst last* order (Fig. 6). The only exception being Cu/Ni$_{200}$ in the *catalyst first* order performing in the range of the *catalyst last* order trials for Cu/Ni$_{500}$ and Cu/Ni$_{600}$. According to the Langmuir-Hinshelwood model, both the reducible moiety (4NP in this case) and the hydride must be on the catalyst surface for the reaction to proceed. In the case of the *catalyst first* approach, 4NP initially adsorbs on the surface before NaBH$_4$ is introduced. In the *catalyst last* approach, the catalyst is introduced to a solution with large excess NaBH$_4$ and likely becomes saturated with surface hydrides where the 4NP must compete for sites before -NO$_2$ reaction can commence, thus resulting in overall lower rate. These findings are commensurate with the general understanding that adsorption of **4NP/4NP*** to the surface is

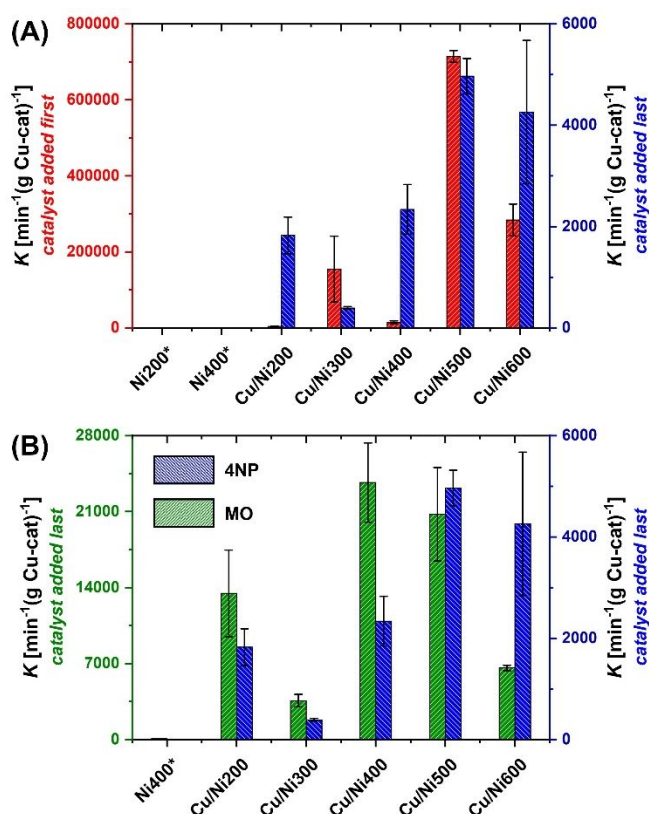the rate limiting step, and further support that the reduction is following the Langmuir-Hinshelwood model.[34]

Fig. 6 (A) Observed catalytic reduction rates for **4NP→4AP** in DIW with excess NaBH$_4$, normalized to Cu catalyst weight; *left = catalyst added first, right = catalyst added last.* (B) Observed catalytic reduction rates for **4NP→4AP** and **MO→4ABS + DMPD** in DIW with excess NaBH$_4$, normalized to Cu catalyst weight with catalyst added last. *Error bars = std. dev.; Observed rates normalized to %Cu species (w/w); *normalized to mass of Ni foam for blank trials.*

Ranking order of catalyst performance for **4NP** reduction changes slightly across the *catalyst first* and *last* orders of addition (Fig. 6A): *catalyst first* (**Cu/Ni$_{200}$** < **Cu/Ni$_{400}$** << **Cu/Ni$_{300}$** ≤ **Cu/Ni$_{600}$** < **Cu/Ni$_{500}$**) and *catalyst last* (**Cu/Ni$_{300}$** << **Cu/Ni$_{200}$** ≤ **Cu/Ni$_{400}$** < **Cu/Ni$_{600}$** < **Cu/Ni$_{500}$**). In general, the CuO materials are more active than Cu$_2$(OH)$_3$Cl, except for **Cu/Ni$_{400}$** which displays peculiarly low (comparative) reactivity in the *catalyst first* approach. This result is surprising given the nominally high BET surface area of 842.09 ± 170.27 m^{2}g^{-1} for the active CuO component. A potential deleterious effect of surface chlorides when comparing **Cu/Ni$_{400}$** to **Cu/Ni$_{500}$** and **Cu/Ni$_{600}$** can be discounted, as they are similarly present in **Cu/Ni$_{300}$** which shows good activity. We postulate that the specific surface morphology of **Cu/Ni$_{400}$** has a high affinity for **4NP** which crowds the surface preventing formation of surface hydrides necessary to promote reduction in the *catalyst first* approach. This trend is reversed and the activity of **Cu/Ni$_{400}$** is relatively enhanced with the *catalyst last* order of addition. We postulate that the discrepancies in ranking order occur due to changes in adsorption affinities of the Cu-material towards **4NP** and BH$_4^-$, which are impacted by material composition (CuO vs

Cu$_2$(OH)$_3$Cl) as well small changes to surface morphology commensurate with calcination temperature. Due to the nature of this material, we cannot, in this study, pinpoint what these specific surface properties are. Similarly, there is no clear indication of surface area effects. Namely, while a large increase in BET surface area is noted going from **Cu/Ni$_{300}$** to **Cu/Ni$_{400}$**, the material also changes from Cu$_2$(OH)$_3$Cl to CuO impairing a meaningful comparison. Additionally, catalysts **Cu/Ni$_{400}$**-**Cu/Ni$_{600}$** display BET surface areas for the active CuO component within error, further obscuring a clear comparison. Nonetheless it is expected that the high surface areas play a role in the overall high reactivity of the respective materials tested; as noted by their comparable reactivity to noble metal systems (*vide infra*).

In general, all catalysts proved to be highly active for the reduction of **MO** to **4ABS** and **DMPD**. In fact, utilizing the slower (but more controlled) *catalyst last* approach, **MO** was reduced approximately 5 times faster when considering the most active catalysts (Table 2). Ranking order of catalyst performance for **4NP** reduction vs **MO** reduction (*both catalyst last order of addition*) yields the following comparison (Fig. 6B): **4NP** (**Cu/Ni$_{300}$** << **Cu/Ni$_{200}$** ≤ **Cu/Ni$_{400}$** < **Cu/Ni$_{600}$** < **Cu/Ni$_{500}$**) and **MO** (**Cu/Ni$_{300}$** < **Cu/Ni$_{600}$** < **Cu/Ni$_{200}$** < **Cu/Ni$_{500}$** ≤ **Cu/Ni$_{400}$**). In going from **4NP** to **MO** we witness a dramatic reversal of performance, where, for example, the activity of **Cu/Ni$_{400}$** significantly increases and that of **Cu/Ni$_{600}$** decreases. This result signifies that the specific temperature of calcination, and in general the preparative route, alters the selectivity of the catalyst towards different functional groups (-NO$_2$ vs -N=N-). One of our groups has previously reported the high specificity of aqueous reduction reactions across different reducible moieties when varying catalyst types, or simply material calcination temperature.[79,80] Ultimately, for the system detailed herein, this implies the opportunity to tune catalyst reactivity towards desired substrate via calcination temperature.

Table 3 Comparison of activity parameter κ for **4NP** and **MO** reduction with NaBH$_4$ in DIW. *Catalyst order of addition: [a] = first, [b] = last.*

| Material	Substrate	K (s^{-1}g^{-1}L)	source
[a]Cu/Ni$_{500}$	4NP	35.72	this work
Cu@g-C$_3$N$_4$	4NP	17.19	ref. 81
Cu$_2$O@CMK-8	4NP	5.57	ref. 82
CuO@CMK-8	4NP	0.14	ref. 82
Cu@ZIF-Co/Zn	4NP	3.83	ref. 83
Au@CeO$_2$	4NP	31.39	ref. 84
Ag-γ-Fe$_2$O$_3$	4NP	3.75	ref. 85
Pd@C$_{amorphous}$	4NP	1.68	ref. 74
Pd@RGO	4NP	13.04	ref. 86
Pd@TiO$_2$	4NP	80.60	ref. 87
Pd@Graphene	4NP	7.85	ref. 88
[b]Cu/Ni$_{400}$	MO	1.18	this work
Cu@ZIF-Co/Zn	MO	1.85	ref. 83
Cu@WB	MO	0.027	ref. 89
Ag-γ-Fe$_2$O$_3$	MO	0.70	ref. 85
Pt@C$_{amorphous}$	MO	0.24	ref. 74
Pd@C$_{amorphous}$	MO	1.36	ref. 74

Conducting a direct comparison of catalytic activity to the literature is complicated by the dependence of k_{app} on a multitude of factors relating to reaction condition; reaction temperature and volume, NaBH$_4$ concentration, mass transport, amount of catalyst used, and the nature and density of active sites, which in most cases remains enigmatic (ours included). However, it is accepted that k_{app} normalized to true catalyst (e.g., active metal in a supported system) weight and reaction volume, dubbed "*activity parameter*" κ (s^{-1}g^{-1}L) enables a practical comparison.[90,91] Though the literature on **4NP** reduction by nanocatalysts is expansive, we highlighted several recent examples germane to our catalyst system, namely the most active Cu-based systems, and other examples of highly reactive precious and semi-precious metal-based systems (Table 3). To facilitate the comparison we compared our most reactive catalyst for **4NP** (**Cu/Ni$_{500}$** - *catalyst first approach*) and similarly for **MO** (**Cu/Ni$_{400}$** - *catalyst last approach*) reduction. In general, catalysts displaying κ in the 1+ s^{-1}g^{-1}L range can be considered very reactive; within the typical domain of precious and semi-precious metal catalysts, and rare examples of extremely reactive base metal systems. For both **4NP** and **MO**, our Ni foam supported CuO catalysts represent both impressive activity compared to not only the best Cu-based systems, but also to highly reactive precious and semi-precious metal systems.

Mechanisms for the reduction of **4NP** on noble metal nanoparticles are frequently proposed, and many aspects have in recent years become substantially better understood.[92-95] Namely, the effects of dissolved oxygen, and the presence of surface-bound ligands.[96-99] A similar level of discussion is lacking in the literature for the reduction of **4NP** by metal oxide catalysts.[100-102] Notably, Chen and coworkers have recently reported the reduction of **4NP** by Co$_3$O$_4$, wherein they observed substantially enhanced activity in samples with increased oxygen vacancies.[103] Generally, defect-driven heterogeneous catalysis is broadly accepted.[104] Based on the recently proposed mechanism from Camargo and coworkers,[105] we propose a tentative mechanism for the reduction of **4NP** at CuO defect sites; namely at O vacancies with neighboring hydroxyl groups (Scheme 2). The presence of surface hydroxyls with neighboring vacancies facilitates the interaction with BH$_4^-$ which (i) generates the necessary surface hydrides, and (ii) operates the parallel hydrolysis sequence to generate H$_2$ – as observed by the continuous formation of bubbles.

Based on our observations, the reaction proceeds according to the Langmuir-Hinshelwood mechanism, necessitating the presence of both the hydride and **4NP*** on the catalyst surface. Upon reduction to the 4-nitrosophenolate (**4NSP***) intermediate, it is desorbed into the solution temporarily. Recently, Xie and coworkers reported the various spectral components pertinent to the **4NP** reaction mechanism. Notably, the appearance of a signal at λ = 265 nm, and a higher intensity absorbance at λ = 395 nm is due to **4NSP***.[106] Upon closer inspection of our UV-Vis spectra, we observe an initial increase and subsequent decrease in absorbance at λ = 265 nm in concert with the decrease in absorbance at λ = 400 nm (Fig. S15-S19). We tentatively attribute this to the expected signal for **4NSP***; the signal at λ = 395 nm is obscured by the broader, higher intensity signal for **4NP*** at λ = 400 nm. At this point, due to the large excess of BH$_4^-$ in the presence of DIW, the surface hydrides and hydroxyls are being continuously regenerated, and upon adsorption of **4NSP*** to the surface, the reduction likely proceeds in a similar manner to ultimately furnish the product **4AP***. The mechanisms of reduction for **MO** on CuO

and both **4NP** and **MO** on $Cu_2(OH)_3Cl$ are currently under investigation. However, based on preliminary findings and adherence to the Langmuir-Hinshelwood model, we postulate a similar defect-mediated pathway operating in parallel to BH_4^- hydrolysis.

regeneration of
Cu-H with $NaBH_4$

regeneration of
Cu-H with $NaBH_4$

regeneration of
Cu-H with $NaBH_4$
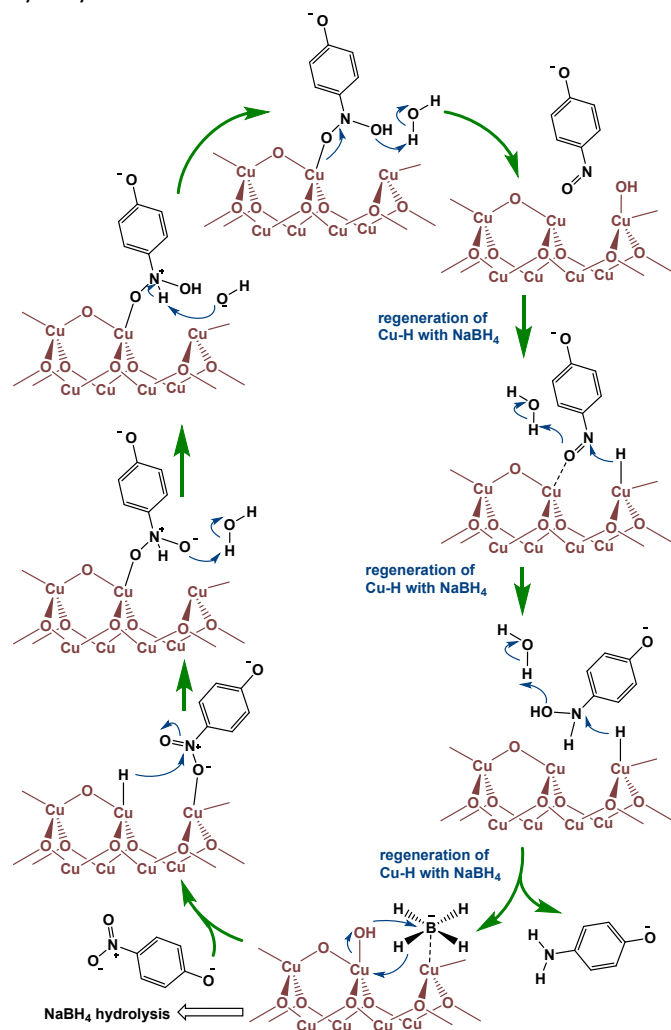
$NaBH_4$ hydrolysis

Scheme 2 Proposed mechanism for the reduction of **4NP*** to **4AP*** in DIW with large excess $NaBH_4$. The large excess of $NaBH_4$ regenerates surface hydrides, and additionally undergoes a hydrolysis side reaction to produce H_2.

3.3 Catalyst recycling

To test the reusability of the catalyst, we conducted a series of recycling trials for the reduction of **4NP** with **Cu/Ni$_{500}$**; the most reactive catalyst from the **4NP** reduction trials noted prior (Fig. S26). The catalytic reactions were conducted under identical conditions as noted prior. Between trials, the catalyst was isolated from the solution by a simple one step physical removal with tweezers (Fig. 1C) and rinsed thoroughly with multiple (3 ×) washes of DIW. Catalytic trials were then repeated. Notably, the catalyst was only rinsed one time with minimal DIW between trials 2 and 3 and again between 4 and 5. The results of the catalytic trials are presented in Figure 7 in two ways: (i) as a function of % change in rate from trial 1 and (ii) as

conventionally reported, % conversion within a specific timeframe (20 min. in this instance). At first glance, it is obvious that trials 3 and 5 exhibit decreased reaction rates and ultimately lower conversion as a result of inadequate rinsing between trials. This result signifies that likely, the **4AP*** product remains adsorbed on the catalyst and inhibits adequate interaction with **4NP*** on the surface, which is required for catalytic turnover, commensurate with the Langmuir-Hinshelwood model (Scheme 2). With a more stringent rinsing protocol, catalyst activity recovers on subsequent trials. Overall, according to conventional metrics, the catalyst clearly retains activity as evident by reproducible % conversion across 8 trials. The steadily decreasing rate over time may be a function of residual material on the catalyst that was not removed between trials. The treatment in between trials is clearly consequential and it is likely that a more optimized process can improve the retention of rate. Overall, the catalyst appears to be robust, very easy to handle and readily recyclable.
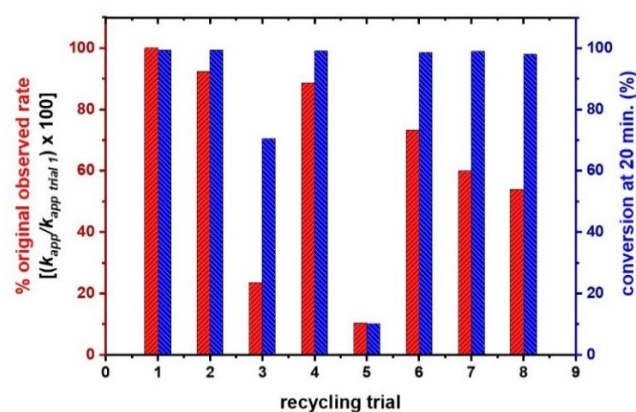

Fig. 7 Recycling trials for the catalytic reduction of **4NP→4AP** in DIW with excess $NaBH_4$, normalized to Cu catalyst weight (**Cu/Ni$_{500}$**). Left = % change in observed rate, right = % conversion at 20 minutes. Trials 1,2,4,6-8 were rinsed thoroughly with DIW, trials 3 and 5 were only cleaned with one quick DIW rinse.

3.4 Catalyst post-mortem

Post-mortem SEM of **Cu/Ni$_{400}$** and **Cu/Ni$_{500}$** after one complete reduction reaction reveals a retention of the porous CuO structures on the Ni foam (Fig. S27). Further XPS and SEM-EDS analysis was conducted on the used **Cu/Ni$_{400}$**; of particular interest was the fate of surface Cl-based contaminants. The pre-catalysis Cu:Cl ratio was 29.8(±9.2):1 (*vide supra*), and after one catalytic reaction, the observed Cu:Cl was 21.0(±5.0):1. The measurements are within error, and any significant difference likely arises from sample-to-sample inhomogeneity. XPS analysis largely aligned with unused **Cu/Ni$_{400}$** material, leading us to conclude that the catalyst remains as predominantly CuO post-use (Fig. S28). The most significant alteration was an increase in the signal intensity at 531 ± 0.1 eV, assigned to oxygen vacancy (O_V);[63] further details on this assignment are noted in section 3.1 (*vide supra*). The generation of surface defects in the form of oxygen vacancies is expected under the $NaBH_4$ rich environment.[103] Of note is the presence of boron on

the surface (atomic % by XPS Cu 2p = 8.21, B 1s = 1.79; Table S9) which results from the hydrolysis of $NaBH_4$. We postulate that build up of boron-based hydrolysis byproduct on the surface ($NaBO_2$ and derivatives thereof) is at least partially responsible for catalyst deactivation; as noted in Fig. 7, more rigorous rinsing protocols between recycling trials led to enhanced recovery of reactivity. Overall, post-reaction, the catalyst appears to retain its morphology and surface chemistry as CuO, with, in the case of **Cu/Ni$_{400}$**, residual Cl.

4. Conclusions

In summary, we have demonstrated a facile and green strategy towards highly-reactive, robust, and easy to handle Ni foam-supported Earth-abundant metal catalysts. The synthetic route requires only modest temperatures for short reaction times, no surfactants or additive redox reagents, DIW as solvent, and simple hydrated $CuCl_2$ salt as precursor. Thus, the preparative route is highly sustainable. The resulting micro-crystalline $Cu_2(OH)_3Cl$ remain well-separated on the Ni foam, and above 400 °C transform to highly porous CuO. All materials display promising activity towards the ubiquitous **4NP** and **MO** aqueous reduction reactions. Additionally, selectivity is impacted by calcination temperature, offering the possibility for tuning by controlling calcination parameters. Our leading CuO-based material (**Cu/Ni$_{500}$**) displays **4NP** reduction rates (35.72 $s^{-1}g^{-1}L$) higher than other reported Cu-based catalysts and is highly competitive with very reactive precious-metal based systems. The integration onto the contiguous Ni foam support allows for facile handling, and as our results indicate, leads to a very robust highly recyclable catalyst, even under the reducing environment of large excess $NaBH_4$. Notably, the exclusion of precious metals, retention of high reactivity, and facile recyclability convene to create a promising sustainable catalyst system.

Author Contributions

L. R. Shultz: investigation, formal analysis, data curation, methodology, visualization, writing - original draft, writing - reviewing and editing, K. Preradovic: investigation, S. Ghimire: investigation, H. Hadley: investigation, S. Xie: investigation, formal analysis, writing – reviewing and editing, data curation, M. J. Beazley, investigation, writing – reviewing and editing, resources, K. Crawford: writing – reviewing and editing, resources, F. Liu: resources, supervision, writing – review and editing, K. Mukhopadhyay: resources, investigation, formal analysis, visualization, writing – original draft, writing – review and editing, supervision, T. Jurca: supervision, resources, conceptualization, funding acquisition, formal analysis, visualization, project administration, methodology, writing – original draft, writing – review and editing.

Conflicts of interest

There are no conflicts to declare.

Acknowledgements

Notes and references

1.   I. C. Gerber and P. Serp, *Chem. Rev.*, 2020, **120**, 1250-1349.
2.   M. J. Valero-Romero, M. Á. Rodríguez-Cano, J. Palomo, J. Rodríguez-Mirasol and T. Cordero, *Front. Mater.,* 2020, **7**, 617432.
3.   N. Zheng and G. D. Stucky, *J. Am. Chem. Soc.*, 2006, **128**, 14278-14280.
4.   J. Seth, P. Dubey, V. R. Chaudhari and B. L. V. Prasad, *New J. Chem.*, 2018, **42**, 402-410.
5.   Y. Wang, C. Wang, L. Wang, L. Wang and F.-S. Xiao, *Acc. Chem. Res.*, 2021, **54**, 2579-2590.
6.   Q. Yang, Q. Xu and H.-L. Jiang, *Chem. Soc. Rev.*, 2017, **46**, 4774-4808.
7.   P. Munnik, P. E. de Jongh and K. P. de Jong, *Chem. Rev.*, 2015, **115**, 6687-6718.
8.   A. N. Pestryakov, V. V. Lunin, A. N. Devochkin, L. A. Petrov, N. E. Bogdanchikova and V. P. Petranovskii, *Appl. Catal. A: Gen.*, 2002, **227**, 125-130.
9.   S. T. Kolaczkowski, S. Awdry, T. Smith, D. Thomas, L. Torkuhl and R. Kolvenbach, *Catal. Today*, 2016, **273**, 221-233.
10.   N. A. Karim, M. S. Alias and H. Yang, *Catalysts*, 2021, **11**, 279.
11.   L. Giani, G. Groppi and E. Tronconi, *Ind. Eng. Chem. Res.*, 2005, **44**, 4993-5002.
12.   A. Gancarczyk, K. Sindera, M. Iwaniszyn, M. Piątek, W. Macek, P. J. Jodłowski, S. Wroński, M. Sitarz, J. Łojewska and A. Kołodziej, *Catalysts*, 2019, **9**, 587.
13.   L. Dou, C. Yan, L. Zhong, D. Zhang, J. Zhang, X. Li and L. Xiao, *Chem. Commun.*, 2020, **56**, 205-208.
14.   J. Teich, R. Dvir, A. Henning, E. R. Hamo, M. J. Moody, T. Jurca, H. Cohen, T. J. Marks, B. A. Rosen, L. J. Lauhon and A. Ismach, *Nanoscale*, 2020, **12**, 2715-2725.
15.   E. O. Pentsak, D. B. Eremin, E. G. Gordeev and V. P. Ananikov, *ACS Catal.*, 2019, **9**, 3070-3081.
16.   W. Zheng, M. Liu and L. Y. S. Lee, *ACS Energy Lett.*, 2020, **5**, 3260-3264.
17.   S. Yuan, L. Cui, X. He, W. Zhang and T. Asefa, *Int. J. Hydrog. Energy*, 2020, **45**, 28860-28869.

18. B. You, N. Jiang, M. Sheng, M. W. Bhushan and Y. Sun, *ACS Catal.*, 2016, **6**, 714-721.

19. Y. Yan, X. Cheng, W. Zhang, G. Chen, H. Li, A. Konkin, Z. Sun, S. Sun, D. Wang and P. Schaaf, *ACS Sustain. Chem. Eng.*, 2019, **7**, 885-894.

20. C. Wang, X. Lv, P. Zhou, X. Liang, Z. Wang, Y. Liu, P. Wang, Z. Zheng, Y. Dai, Y. Li, M.-H. Whangbo and B. Huang, *ACS Appl. Mater. Interfaces*, 2020, **12**, 29153-29161.

21. Y. J. Son, K. Kawashima, B. R. Wygant, C. H. Lam, J. N. Burrow, H. Celio, A. Dolocan, J. G. Ekerdt and C. B. Mullins, *ACS Nano*, 2021, **15**, 3468-3480.

22. H. Cao, Z. Li, Y. Xie, F. Xiao, H. Wang, X. Wang, K. Pan and A. Cabot, *ChemSusChem*, 2021, **14**, 1094-1102.

23. M.-H. Tsai, T.-C. Chen, Y. Juang, L.-C. Hua and C. Huang, *Electrochem. Commun.*, 2020, **121**, 106875.

24. M. I. Abdullah, A. Hameed, N. Zhang, M. H. Islam, M. Ma and B. G. Pollet, *ACS Appl. Mater. Interfaces*, 2021, **13**, 30603-30613.

25. P.-P. Tang, X. Lin, H. Yin, D.-X. Zhang, H. Wen, J.-J. Wang and P. Wang, *ACS Sustain. Chem. Eng.*, 2020, **8**, 16583-16590.

26. G. Wang, D. Cao, C. Yin, Y. Gao, J. Yin and L. Cheng, *Chem. Mater.*, 2009, **21**, 5112-5118.

27. F. Wang, Y. Luo, Y. Zhang, Y. Wang and H. Zhu, *Energy Fuels*, 2020, **34**, 11365-11372.

28. T. Xie, W. Luo, Z. Zhou, W. Sun, Q. Wang, L. Cao and J. Yang, *ACS Omega*, 2019, **4**, 21340-21345.

29. K. Zha, W. Sun, Z. Huang, H. Xu and W. Shen, *ACS Catal.*, 2020, **10**, 12127-12138.

30. M. Feng, Z.-H. Luo, S. Yi, H. Lu, C. Lu, C.-Y. Li, J.-L. Zhao and G.-P. Cao, *Ind. Eng. Chem. Res.*, 2018, **57**, 16227-16238.

31. H. Yang, J. Li, H. Yu, F. Peng and H. Wang, *Int. J. Chem. React.*, 2015, **13**, 83-93.

32. A. Sirijaruphan, J. G. Goodwin Jr, R. W. Rice, D. Wei, K. R. Butcher, G. W. Roberts and J. J. Spivey, *Appl. Catal. A: Gen.*, 2005, **281**, 1-9.

33. P. Herves, M. Pérez-Lorenzo, L. M. Liz-Marzan, J. Dzubiella, Y. Lu and M. Ballauff, *Chem. Soc. Rev.*, 2012, **41**, 5577-5587.

34. T. Aditya, A. Pal and T. Pal, *Chem. Commun.*, 2015, **51**, 9410-9431.

35. S. Yi, W.-Q. Zhuang, B. Wu, S. T.-L. Tay and J.-H. Tay, *Environ. Sci. Technol.*, 2006, **40**, 2396-2401.

36. J. Xia, G. He, L. Zhang, X. Sun and X. Wang, *Appl. Catal. B: Environ.*, 2016, **180**, 408-415.

37. M. R. H. Podeh, S. K. Bhattacharya and M. Qu, *Water Res.*, 1995, **29**, 391-399.

38. H. Zhao and C.-H. Kong, *Chemical Eng. J.*, 2018, **339**, 424-431.

39. M. Sun, D. D. Reible, G. V. Lowry and K. B. Gregory, *Environ. Sci. Technol.* 2012, **46**, 6174-6181.

40. A. Sahoo and S. Patra, *ACS Appl. Nano Mater.*, 2018, **1**, 5169-5178.

41. K.-S. Ju and R. E. Parales, *Microbiol. Mo. Biol. Rev.*, 2010, **74**, 250-272.

42. Z. Xiong, H. Zhang, W. Zhang, B. Lai and G. Yao, *Chem. Eng. J.*, 2019, **359**, 13-31.

43. C.-F. Hsia, M. Madasu and M. H. Huang, *Chem. Mater.*, 2016, **28**, 3073-3079.

44. F. Wang, W. Li, X. Feng, D. Liu and Y. Zhang, *Chem. Sci.*, 2016, **7**, 1867-1873.

45. T. Kim, X. Fu, D. Warther and M. J. Sailor, *ACS nano*, 2017, **11**, 2773-2784.

46. A. Liu, L. Yang, C.-H. Traulsen and J. Cornelissen, *Chem. Commun.*, 2017, **53**, 7632-7634.

47. E. Menumerov, R. A. Hughes and S. Neretina, *Catal. Sci. Technol.*, 2017, **7**, 1460-1464.

48. E. Menumerov, R. A. Hughes, S. D. Golze, R. D. Neal, T. B. Demille, J. C. Campanaro, K. C. Kotesky, S. Rouvimov and S. Neretina, *ACS Catal.*, 2018, **8**, 8879-8888.

49. L. R. Shultz, C. Feit, J. Stanberry, Z. Gao, S. Xie, V. A. Anagnostopoulos, F. Liu, P. Banerjee and T. Jurca, *Catalysts*, 2021, **11**, 165.

50. C. Huang, W. Ye, Q. Liu and X. Qiu, *ACS Appl. Mater. Interfaces*, 2014, **6**, 14469-14476.

51. Y.-g. Wu, M. Wen, Q.-s. Wu and H. Fang, *J. Phys. Chem. C*, 2014, **118**, 6307-6313.

52. D. Formenti, F. Ferretti, F. K. Scharnagl and M. Beller, *Chem. Rev.*, 2018, **119**, 2611-2680.

53. X. Wang, J. Lu, Y. Zhao, X. Wang, Z. Lin, X. Liu, R. Wu, C. Yang and X. Su, *ChemCatChem*, 2018, **10**, 4143-4153.

54. L. Gao, R. Li, X. Sui, R. Li, C. Chen and Q. Chen, *Environ. Sci. Technol.*, 2014, **48**, 10191-10197.

55. J. Zhang, F. Zhang, Y. Yang, S. Guo and J. Zhang, *ACS Omega*, 2017, **2**, 7293-7298.

56. D. V. Shtansky, K. L. Firestein and D. V. Golberg, *Nanoscale*, 2018, **10**, 17477-17493.

57. S. Wolf and C. Feldmann, *J. Mater. Chem.*, 2010, **20**, 7694-7699.

58. M. Verma, V. Kumar and A. Katoch, *Mater. Sci. Semicond. Process.*, 2018, **76**, 55-60.

59. C. Engelbrekt, P. Malcho, J. Andersen, L. Zhang, K. Ståhl, B. Li, J. Hu, J. Zhang, *J. Nanopart. Res.,* **16**, 1-12.

60. S. A. Khromova, A. A. Smirnov, O. A. Bulavchenko, A. A. Saraev, V. V. Kaichev, S. I. Reshetnikov and V. A. Yakovlev, *Appl. Catal. A: Gen.*, 2014, **470**, 261-270.

61. M. C. Biesinger, *Surf. Interface. Anal.*, 2017, **49**, 1325-1334.

62. A. Jha, D.-W. Jeong, J.-O. Shim, W.-J. Jang, Y.-L. Lee, C.V. Rode, H.-S. Roh, *Catal. Sci. Technol.,* 2015, **5** ,2752-2760.

63. A. Kushwaha, M. Aslam, *J. Phys. D Appl. Phys.*, 2013, **46**, 485104.

64. T. Kenji, Y. Hirano, E. Suzuki, *Appl. Catal. A: Gen.,* 1998, **170**, 245-254.

65. D. Gao, Z. Yang, J. Zhang, G. Yang, Z. Zhu, J. Qi, M. Si, D. Xue, *AIP Adv.,* 2011, **1**, 042168.

66. S. Wang, H. Yang, X. Yi, H. M. K. Sari, X. Zhang, T. Wang, Z. Zou, B. Cao, J. Qin, J. Wang, W. Li, X. Li. *Appl. Surf. Sci.*, 2022, **574**, 151649.

67. J. C. Dupin, D. Gonbeau, P. Vinatier, A. Levasseur, *Phys. Chem. Chem. Phys.*, 2000, **2**, 1319-1324.

68. Y. Wang, Y. Lü, W. Zhan, Z. Xie, Q. Kuang, L. Zheng, *J. Mater. Chem. A,* 2015, **3**, 12796-12803.

69. W.-T. Park, I. Son, H.-W. Park, K.-B. Chung, Y. Xu, T. Lee, Y.-Y. Noh, *ACS Appl. Mater. Interfaces*, 2015, **7**, 13289-13294.

70. E. Cano, C. Torres, J. Bastidas, *Mater. Corros.*, 2001, **52**, 667-676.

71. M. C. Biesinger, B. P. Payne, A. P. Grosvenor, L. W. Lau, A. R. Gerson and R. S. C. Smart, *Appl. Surf. Sci.*, 2011, **257**, 2717-2730.

72. W. Wei, P. Gao, J. Xie, S. Zong, H. Cui and X. Yue, *J. Solid. State. Chem.*, 2013, **204**, 305-313.

73. I. U. Haq, K. Akhtar, K. Mallok, *Mater. Res. Bull.*, 2014, **57**, 121-126.

74. L. R. Shultz, L. Hu, K. Preradovic, M. J. Beazley, X. Feng and T. Jurca, *ChemCatChem*, 2019, **11**, 2590-2595.

75. A. K. Ilunga, T. Khoza, E. Tjabadi and R. Meijboom, *ChemistrySelect*, 2017, **2**, 9803-9809.

76. F. Ali, S. B. Khan, T. Kamal, K. A. Alamry and A. M. Asiri, *Sci. Rep.*, 2018, **8**, 1-18.

77. S. R. Thawarkar, B. Thombare, B. S. Munde and N. D. Khupse, *RSC Adv.*, 2018, **8**, 38384-38390.

78. M. Kaloti and A. Kumar, *ACS Omega*, 2018, **3**, 1529-1545.

79. L. R. Shultz, B. McCullough, W. J. Newsome, H. Ali, T. E. Shaw, K. O. Davis, F. J. Uribe-Romo, M. Baudelet and T. Jurca, *Molecules*, 2020, **25**, 89.

80. L. R. Shultz, L. Hu, X. Feng and T. Jurca, *ChemPhysChem*, 2020, **21**, 1627-1631.

81. S. Huang, Y. Zhao and R. Tang, *RSC Adv.*, 2016, **6**, 90887-90896.

82. P. C. Rath, D. Saikia, M. Mishra and H.-M. Kao, *Appl. Surf. Sci.*, 2018, **427**, 1217-1226.

83. C. S. Budi, J. R. Deka, W.-C. Hsu, D. Saikia, K.-T. Chen, H.-M. Kao and Y.-C. Yang, *J. Hazard. Mater.*, 2021, **407**, 124392.

84. C.-M. Fan, L.-F. Zhang, S.-S. Wang, D.-H. Wang, L.-Q. Lu and A.-W. Xu, *Nanoscale*, 2012, **4**, 6835-6840.

85. S. Sallam, G. El-Subruiti and A. Eltaweil, *Catal. Lett.*, 2018, **148**, 3701-3714.

86. S. Hemmati, L. Mehrazin, H. Ghorban, S. H. Garakani, T. H. Mobaraki, P. Mohammadi and H. Veisi, *RSC Adv.*, 2018, **8**, 21020-21028.

87. M. Imran, A. B. Yousaf, X. Zhou, Y.-F. Jiang, C.-Z. Yuan, A. Zeb, N. Jiang and A.-W. Xu, *J. Phys. Chem. C*, 2017, **121**, 1162-1170.

88. J. Sun, Y. Fu, G. He, X. Sun and X. Wang, *Catal. Sci. Technol.*, 2014, **4**, 1742-1748.

89. H. S. M. Ali and S. A. Khan, *ACS omega*, 2020, **5**, 7379-7391.

90. L. R. Lara, A. D. Zottis, W. C. Elias, D. Faggion, C. E. M. de Campos, J. J. S. Acuña and J. B. Domingos, *RSC Adv.*, 2015, **5**, 8289-8296.

91. C. Kästner and A. F. Thünemann, *Langmuir*, 2016, **32**, 7383-7391.

92. S. Wunder, F. Polzer, Y. Lu, Y. Mei and M. Ballauff, *The J. Phys. Chem. C*, 2010, **114**, 8814-8820.

93. X. Kong, H. Zhu, C. Chen, G. Huang and Q. Chen, *Chem. Phys. Lett.*, 2017, **684**, 148-152.

94. S. Gu, S. Wunder, Y. Lu, M. Ballauff, R. Fenger, K. Rademann, B. Jaquet and A. Zaccone, *J. Phys. Chem. C*, 2014, **118**, 18618-18625.

95. D. Besold, S. Risse, Y. Lu, J. Dzubiella and M. Ballauff, *Ind. Eng. Chem. Res.*, 2021, **60**, 3922-3935.

96. J. Strachan, C. Barnett, A. F. Masters and T. Maschmeyer, *ACS Catal.*, 2020, **10**, 5516-5521.

97. R. D. Neal, Y. Inoue, R. A. Hughes and S. Neretina, *J. Phys. Chem. C*, 2019, **123**, 12894-12901.

98. R. D. Neal, R. A. Hughes, P. Sapkota, S. Ptasinska and S. Neretina, *ACS Catal.*, 2020, **10**, 10040-10050.

99. E. Menumerov, R. A. Hughes and S. Neretina, *Nano Lett.*, 2016, **16**, 7791-7797.

100. Y. Su, J. Lang, L. Li, K. Guan, C. Du, L. Peng, D. Han and X. Wang, *J. Am. Chem. Soc.*, 2013, **135**, 11433-11436.

101. J.-L. Ortiz-Quiñonez and U. Pal, *ACS Omega*, 2019, **4**, 10129-10139.

102. A. Chinnappan, S. K. Eshkalak, C. Baskar, M. Khatibzadeh, E. Kowsari and S. Ramakrishna, *Nanoscale Adv.*, 2019, **1**, 305-313.

103. H. Chen, M. Yang, S. Tao and G. Chen, *Appl. Catal. B: Environ.*, 2017, **209**, 648-656.

104. C. Xie, D. Yan, H. Li, S. Du, W. Chen, Y. Wang, Y. Zou, R. Chen and S. Wang, *ACS Catal.*, 2020, **10**, 11082-11098.

105. E. C. M. Barbosa, J. L. Fiorio, T. Mou, B. Wang, L. M. Rossi and P. H. C. Camargo, *Chem. Eur. J.*, 2018, **24**, 12330-12339.

106. R. R. Nasaruddin, T. Chen, J. Li, N. Goswami, J. Zhang, N. Yan and J. Xie, *ChemCatChem*, 2018, **10**, 395-402.